RESEARCH ON A NOVEL CONCEPT OF SELF-FORMING AIR COOLING BATTERY RACK

Mingjie Zhang[a], Kai Yang[a], Le Qin[b], Xiaole Yao[b], Qian Liu[b], Xing Ju[b,*]

[a] State Key Laboratory of Operation and Control of Renewable Energy & Storage Systems（China Electric Power Research Institute）
[b] Key Laboratory of Power Station Energy Transfer Conversion and System of MOE, North China Electric Power University, Beijing 102206, PR China

ABSTRACT

Lithium-ion batteries used for energy storage systems will release amount of heat during operation. It will cause serious consequences of thermal runaway if not dissipate in time. In this study, a self-forming air-cooled battery rack of the energy storage system is established based on the normal battery rack for energy storage and the shape of the energy storage battery itself. The frames of the battery rack acts as air ducts, which greatly reduce the system complexity. In this paper, the heat generation model is established based on the experiment, and the four battery rack forms are studied by CFD simulation. The flow uniformity of the two-level shunt structure, the maximum temperature of the battery, the temperature difference and the overall pressure drop of the battery rack are analyzed. It was found that the self-forming battery rack in the form of Case IV has the highest flow rate and temperature uniformity due to the tapered air ducts. Case IV can also resist flow non-uniformity when increase the flow rate. The maximum temperature can be maintained at 33.8 ℃ at 0.5 C under the 46 g/s flowrate. Where the maximum bulk temperature difference between batteries and inside a single battery is less than 3.8 ℃ and 1 ℃, respectively. The pressure drop is only 4.8 Pa. What's more, Case IV achieves optimal cooling performance at a 92 g/s flow rate, under which the maximum bulk temperature is 31.8 ℃ with the pressure drop of 19.5 Pa.

Keywords: *Lithium ion battery, battery thermal management system, air cooling, self-forming*

1. INTRODUCTION

Along with the popularity of renewable energy and the construction of smart grids, the technology of energy storage systems (ESS) has been developed rapidly (Fathima and Palanismay 2017). In particular, lithium-ion battery (LIB) energy storage system has developed and matured by leaps and bounds. This also brings about the increasing safety requirements (Ashkboos *et al*. 2021; Killer *et al*. 2020; Tao *et al*. 2020). However, with the increasing capacity and battery density of ESS, a simple air-conditioning system can no longer meet the high heat flux of a lithium-ion battery container storage system (Kalogiannis *et al*. 2022; Schimpe *et al*. 2018). The capacity and life of lithium-ion batteries significantly influence the service life and endurance of containers (Bandhauer *et al*. 2011). Due to the small gap between the battery array in the container, the heat is difficult to be dissipated quickly. Accumulated heat causes a large temperature difference between battery packs, which leads to inconsistent internal resistance and capacity and increases safety risks. The acceptable operating temperature range of the lithium-ion battery is −20 °C to 60°C (Väyrynen and Salminen 2012). A low-temperature environment causes electrolyte solidification and impedance to increase (Piao *et al*. 2022). The high temperature greatly reduces the capacity and cycle life, increasing the risk of battery thermal runaway. Also noteworthy is that the maximum temperature difference between cells and modules in the battery pack should be less than 5 °C (Pesaran 2002). Therefore, LIB-based ESS needs an efficient battery thermal management system (BTMS) to dissipate the heat rapidly. There are several cooling approaches for LIBs: liquid cooling, phase change material cooling, heat pipe cooling, and air cooling.

Liquid coolants are a more attractive cooling medium due to their higher thermal conductivity. Liquid cooling includes direct cooling and indirect cooling. Direct cooling immerses the cell modules in coolant such as oil, while indirect cooling is achieved by fluid flowing through discrete pipes or jackets around the cells. For indirect liquid cooling, high thermal resistance exists because of the thickness of the pipes or plates. To improve the heat transfer efficiency, small channels can be used (Lan *et al*. 2016), or the high thermal conductivity flexible graphite can be inserted between the batteries and the pipes (Zhang *et al*. 2017). Tong *et al*. (Tong *et al*. 2015) improved average temperature and temperature uniformity by increasing coolant flowrate and plate thickness. However, this increases the pumping power consumption. For direct liquid cooling, the coolant is in direct contact with the battery, which makes cooling more efficient. However, considering the electrical insulation requirements, the coolant must be replaced frequently. In addition, for the LIB container storage system, the liquid cooling system has a heavyweight and structural complexity. What's more, liquid cooling has low economic benefit, high technical difficulty in installation and subsequent maintenance, and the potential risk of coolant leakage, so it cannot be widely used in LIB container storage systems.

Phase change material (PCM) can store and release heat during the melting and solidification process while keeping the temperature nearly constant. Therefore, it can be used to warm up the battery or slow down the battery's temperature drop during short-term of parking in a cold environment (Lei *et al*. 2020) and avoid damage or deterioration. Immersing PCM into porous media has been a research hotspot in the past few years (Le *et al*. 2022). Wang *et al*. (Wang *et al*. 2015) added aluminum foam to the PCM system and improved the PCM's thermal storage and thermal conductivity. What's more, after adding paraffin-

foam aluminum material, the PCM's thermal conductivity is increased from 0.29 W/(K·m) to 46.12 W/(K·m). Hussain *et al.* (Hussain *et al.* 2016) added nickel foam to PCM. Compared with natural air and pure PCM cooling system, the temperature of using composite PCM cooling systems was reduced by 31% and 24%, respectively. However, when all the solid PCM converts to liquid, there is a high thermal resistance between the battery and PCM. The cooling performance becomes even worse than direct air cooling. Therefore, PCM cooling is frequently paired with other cooling technologies (i.e. forced air cooling and liquid cooling) to solidify the PCM and recover its latent heat. Hemery *et al.* (Hémery *et al.* 2014) proposed a hybrid BTMS combining a PCM system with a forced liquid cooling system. The PCM remained fully solid-state under 1 oC charge rate using only 400 W of pump power. However, the volume changes in solidification and melting during the PCM cooling system operating process. Also, the large weight makes it unsuitable for the transportation and installation of the LIB container storage system.

Heat pipe cooling can arbitrarily change shape to suit the heat transfer. Heat pipe has the advantages of the lightweight, low cost, no maintenance, and high thermal conductivity. The choice of coolant has a great influence on the cooling effect and safety of the heat pipe, such as deionized water, ethanol, and acetone. The cooling mode of the condenser end (Zhao *et al.* 2015) and the inclined position of the heat pipe (Tran *et al.* 2014) also affect its performance. However, due to the low capacity, low efficiency, and small contact area, heat pipe has not yet been applied to the main application of BTMS (Kim *et al.* 2019).

Air cooling is a traditional method, including natural cooling and forced cooling (Rao and Wang 2011). In general, the convective heat transfer coefficient of natural air cooling is much lower than that of forced air cooling. Therefore, natural convection cooling is only effective for low discharge rate applications, such as mobile phones. Recently, the improvement of forced air cooling has mainly focused on the geometry structure and parameter optimization. Park *et al.* (Park 2013) found that the maximum temperature of the conical manifold was much lower than others, and this conclusion was verified in Ref (Sun and Dixon 2014). The conical flow ducts with orifices and the corrugations between the cooling plates significantly improved flow distribution uniformity. In addition, independent air ducts, fans, and distributed fine air ducts (Fathabadi 2014) can both make the battery pack obtain a uniform temperature. Hong *et al.* (Hong *et al.* 2018) studied the influence on the cooling performance of BTMS by changing the position and size of the additional secondary exhaust port on the outlet duct wall. Xie *et al.* (Xie *et al.* 2017) studied the influence of inlet/outlet air duct angles and widths to optimize air cooling structure and reduce the maximum temperature difference and maximum temperature of the battery pack. In addition, parameters such as battery spacing (Yang *et al.* 2015) and air volume flow rate (Fan *et al.* 2013) are also being studied. Saw *et al.* (Saw *et al.* 2016) used the CFD method to numerically study the thermal behavior of air-cooled battery packs, and derived the exponential expression between Nusselt number and Reynolds number to predict the cooling performance of BTMS. Zhu *et al.* (Zhu *et al.* 2013) studied the optimal fan power to balance the cost and compactness using the proposed electrochemical thermal model. Wang *et al.* (Wang *et al.* 2015) introduced an empirical heat source based three-dimensional model to investigate the thermal behaviors of the 5 ×5 cells module under different conditions. The heat generation rate in the thermal model was measured experimentally under the adiabatic condition. Tong *et al.* (Tong *et al.* 2016) developed a thermo-electrochemical model to explore the thermal performance of forced air cooling under different cooling conditions. The factors including the air inlet velocity, cells arrangement, cell spacing, and reversal frequency were all considered.

The aforementioned researches show that liquid cooling, PCM, and heat pipe cooling are not suitable for LIB energy storage system due to large volume, easy leakage of cooling medium, high price, and system complexity. While air cooling is an ideal BTMS choice of LIB container storage system. Nowadays, most LIB container storage systems use air conditioning as BTMS, which cannot accurately control single battery

cells. At the same time, the air conditioning system and the ESS are independent of each other and need to be arranged separately. This results in the low efficiency of space utilization, which reduces the capacity of LIB container storage systems. To tackle this issue, a novel self-forming air cooling battery rack for energy storage batteries is proposed here. The self-forming rack solves the problem of temperature non-uniformity of the battery in the rack through flow reforming. The current work analyzes the flow state and temperature uniformity over the four cases. Moreover, for the best model, the monitoring of discharge temperature and the influence of the flow rate are investigated. The air-cooling self-forming approach proposed in this paper does not require an additional mechanism. It arranges the flow channels based on the battery rack shape to achieve a highly integrated ESS. Accordingly, air-cooled self-forming rack well solves the thermal management problem of large-scale LIB energy storage systems.

2. MODEL

This section describes the physical model, battery heat generation model and calculation model used in this paper, and verifies the model reliability by experiment.

2.1 Physical model

Air conditioning is the main thermal management method of energy storage containers, which provides hot air in a low temperature environment and cold air in high temperature environment. This provides a suitable temperature for batteries working in the container. However, it needs to add an additional air conditioning system. Besides, the forced convection provided by the air conditioning is limited and cannot accurately control the temperature of each battery cell. It's hard to get a uniform temperature for each battery. Therefore, this paper proposes a new cooling scheme for the energy storage system and designs the air duct based on the shape of the battery rack.
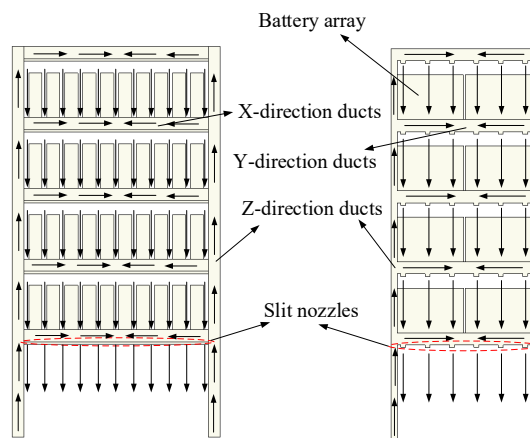

Fig. 1. Schematic diagram of battery cooling duct structure

As shown in Fig. 1, the battery rack has four layers, and each of them carries 20 batteries. The support framework serves as the cooling air duct. Cooling air flows in from the four Z-direction ducts' bottom surfaces and flows upwards. Each Z-direction duct is arranged with five equidistant Y-direction ducts, which divide the rack into four layers, and each Y-direction duct has six equidistant X-direction ducts with nozzles below them. During the cooling process, air flows up from the Z-direction ducts and then into the Y-direction ducts of each layer. Finally, air flows into the X-direction ducts. The air flows down from nozzles below each X-direction duct and through the battery spacing of the battery array. The heat generated by the battery is not only taken away by the air jet from the nozzle of the upper X-direction ducts but also exported by the X-direction ducts' internal air that supports the battery. The air that flows into the external open space can also reduce the temperature inside the

container. The advantage of this cooling configuration is that no extra system is added; the flow pattern is reconfigured according to the inherent form of the rack itself. The self-forming battery air cooling rack forms air jets flowing through the battery spacing, which strengthens convection heat transfer efficiency.

2.2 Experiment and heat generation model

The battery heat generation model used in this investigation is the Bernardi equation. The flow pattern design and optimization are done using CFD. The materials and battery data used are listed in Table 1.

Table 1 The thermal-physical parameters of the battery cell, air and aluminum.

	Battery	Aluminum	Air
ρ, kg/m3	2064	2719	998.2
Cp, J /(kg·K)	1068	871	4182
Battery capacity, Ah	51	—	—
λ, W/(m·K)	X:2.13 Y:11.3 Z:11.3	202.4	0.6

During the discharge process, the temperature rise caused by electrochemical reaction inside the battery is called reversible heat q_{rev}, and the temperature rise caused by internal resistance is called irreversible heat q_{irr}.

Heat generation rate q_{gen} can be expressed as:

$$q_{gen} = q_{rev} + q_{irr} \tag{1}$$

q_{rev} and q_{irr} can be expressed as:

$$q_{rev} = -\frac{IT_{bat}}{V_{bat}} \cdot \frac{\partial OCV}{\partial T_{bat}} \tag{2}$$

$$q_{irr} = \frac{I^2 R_e}{V_{bat}} \tag{3}$$

$$R_e = \frac{OCV - U}{I} \tag{4}$$

In the formula, I, T_{bat}, OCV, R_e and U are the discharge current, battery temperature during discharge, open-circuit voltage, battery internal resistance, voltage and battery entropy coefficient, respectively. So q_{gen} can be written as (Basu *et al*. 2016; Gümüşsu *et al*. 2017; Mahamud and Park 2011; Zhou *et al*. 2019)：

$$q_{gen} = \frac{I}{V_{bat}}\left[(OCV - U) - T_{bat}\frac{\partial OCV}{\partial T_{bat}}\right] \tag{5}$$

The heat generated by the battery is defined as a constant heat source and calculated by Eq. (5). To obtain the actual heat release characteristics of the battery, a 50 Ah prismatic lithium-ion battery test system was built. The test system includes a battery charge and discharge tester (CT-4008-5V60A-NTA), an Agilent Data acquisition to collect battery surface temperature, and a constant temperature and humidity chamber to ensure a constant temperature environment for the battery (EH-1000L-C3, temperature range: -40°C ~ 150°C, humidity range: 20%R.H ~ 98%R.H), and three K-type thermocouples. The thermocouples are placed at the positions shown in Fig. 2 to measure the battery's temperature distribution, and the ambient temperature was 25°C. The experimental device schematic diagram is shown in Fig. 2.

Table 2 Heat production at different C-rates

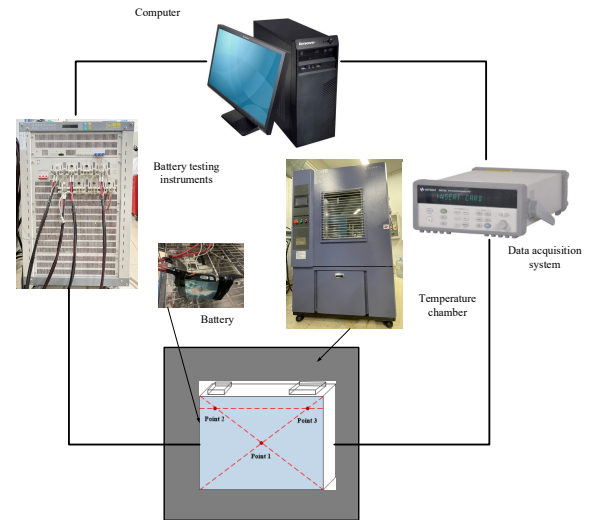| C-rate	Current, A	Heat generation power, W
0.5	24	3.67
1	48	12.16
2	96	48.64
3	144	109.44
4	192	194.57

Fig. 2 Schematic diagram of the experimental platform

The hybrid pulse power characterization test (HPPC) (Lou *et al*. 2012) and potentiometric method (Zhang *et al*. 2014) of the battery is applied. The results showed that the internal resistance and the corresponding entropy coefficient of battery discharge both changed with the SOC, and the relationships are as following equations:

$$R_e = 0.00637 - 0.00894*(SOC) + 0.01423*SOC^2 - 0.00774*SOC^3 \tag{6}$$

$$\frac{\partial OCV}{\partial T_{bat}} = (-0.0002147 + 0.00165338*(SOC) - 0.00166174*SOC^2 + 0.00625276* \tag{7}$$

$$SOC^3 - 0.03419254*SOC^4 + 0.05306229*SOC^5 - 0.0251684*SOC^6$$

Substituting the Eq. (6) and Eq. (7) into the Bernardi equation Eq. (5), we obtain the relationship of battery heat generation rate with SOC. At the same time, the equation is compiled as UDF source term in FLUENT numerical calculation. The heat generation curves at different discharge temperatures at 25 °C natural convection are compared between the experimental data and simulation results, as depicted in Fig. 3.
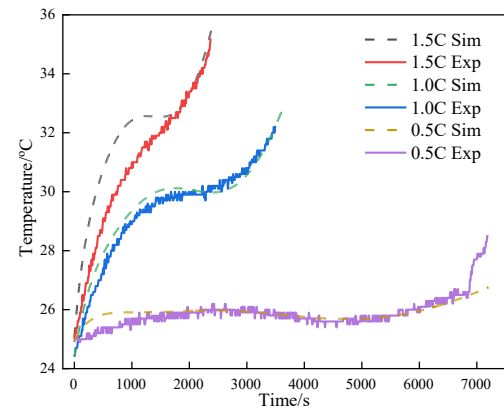

Fig. 3 Comparison of experimental and simulated temperature curves with time

It can be seen that the temperature curve of the simulation result fits well with the experimental data, and the error is less than 0.4%. Therefore, the present model can be used for the subsequent computation. Using constant heat generation in structural optimization, the average values of internal resistance and corresponding entropy coefficient are 4.902 mΩ and 0.0009 mV/K, respectively. The heat generation power at different discharge rates is demonstrated in the following Table 2.

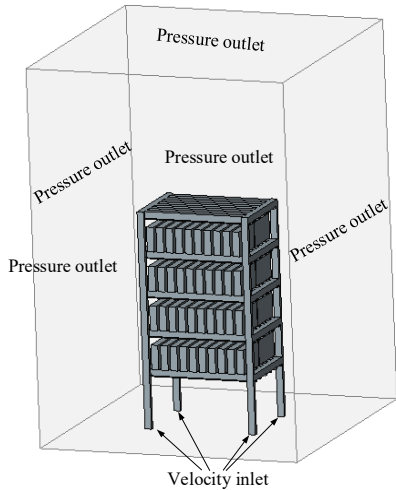## 2.3 Numerical simulation model

Fig. 4 Schematic diagram of the computational domain

The proposed model of the battery rack is depicted in Fig. 4. The battery rack is in an open space, and the pressure outlet boundary is set on the surrounding surfaces, while the bottom surface is set as an adiabatic wall. The inlet boundary condition is set as velocity inlet, the initial flow rate is set at 46 g/s, and the boundary equations are defined as follows:.

adiabatic boundary:
$$-\lambda_{bat}\left(\frac{\partial T_{bat.}}{\partial n}\right) = 0 \tag{9}$$

solid-gas coupling surface:
$$-\lambda_{bat}\left(\frac{\partial T_{bat}}{\partial n}\right) = -\lambda_a\left(\frac{\partial T_a}{\partial n}\right); \quad T_{bat,wall} = T_{a,wall} \tag{10}$$

velocity inlet: $v_x = v_y = 0, v_z = v_0, T_a = T_0$ (11)

pressure outlet: $\left(\frac{\partial \vec{v}}{\partial n}\right) = 0$ (12)

The Reynolds number (*Re*) of the air in the calculation is greater than 2300, so the turbulence model is active. The *k-e* realizable model and the open scalable wall function are also active. The following assumptions are considered in the present modeling:
1. The battery is a uniform heat source, and the heat generation is constant at 3.67 W.
2. Air is incompressible and its physical properties are time independent.
3. The air inlet direction is perpendicular to the inlet surface.
4. There is no slip between air and the wall contact surface.

The momentum, energy, and continuity conservation equations are described as follows:

$$\frac{\partial \rho_a}{\partial \tau} + \nabla \cdot (\rho_a \vec{v}) = 0 \tag{13}$$

$$\frac{\partial}{\partial \tau}(\rho_a c_a T_a) + \nabla \cdot (\rho_a c_a T_a \vec{v}) = -\nabla \cdot (\lambda_a \nabla T_a) \tag{14}$$

$$\frac{\partial}{\partial \tau}(\rho_a \vec{v}) + \nabla \cdot (\rho_a \vec{v}\vec{v}) = -\nabla P + \frac{\mu}{\rho_a}\nabla^2 \vec{v} + \rho_a g \tag{15}$$

Grid independence was verified before calculation. As shown in Fig. 5, due to the slight number of cells in grid 1, the conservation equations cannot converge. Whereas the obtained results from grid 4 and grid 3 differ by less than 1%, thus the mesh of grid 3 that containing 15456806 cells is adopted for subsequent computations. The grid used for calculation in this paper is shown in Fig. 6. The grid of the battery rack is encrypted to capture air turbulence characteristics.
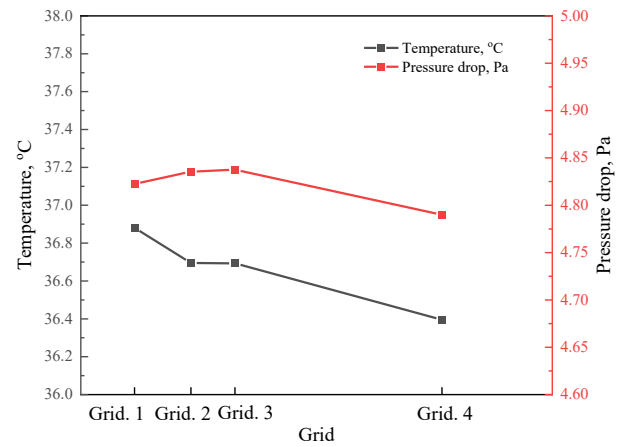

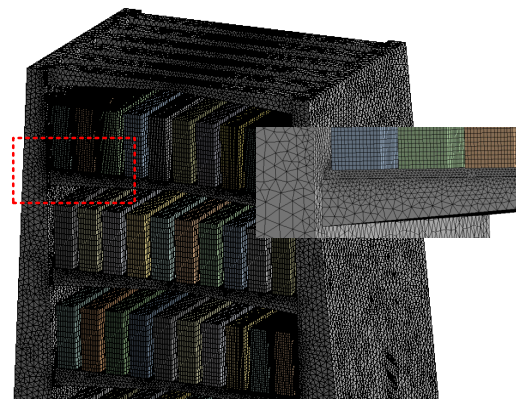**Fig. 5** Temperature and pressure drop curves with the number of grids
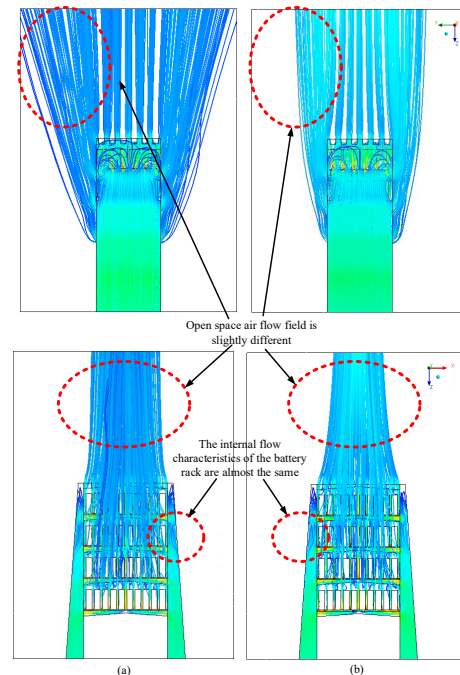

Fig. 6 Grid used in calculation

Fig. 7 Calculation result with (a)active and (b) inactive Boussinesq's Hypothesis

The verification of whether the Boussinesq's Hypothesis is necessary to be turned on is carried out before the calculation. As can be seen in Fig. 7, the opening or not of the Boussinesq's Hypothesis has a slight influence on the air flow field in the open space. But it has little influence on the capture of flow characteristics inside the battery rack. This is because the natural convection can be almost ignored in forced flow. And whether the Boussinesq's Hypothesis is turned on has little influence on the maximum temperature and voltage drop of the battery. Compared between open and not open the Boussinesq's Hypothesis, the T_{max} of the model has 0.2 °C difference and pressure drop is the same. This paper mainly studies the cooling performance of the battery rack, and does not require too much about the characteristics of the opening space. Therefore, in order to accelerate the convergence and reduce the calculation cost, the Boussinesq's Hypothesis is not active in the calculation.

3. RESULT AND DISCUSSION

This section conducts the numerical calculation on the cooling structure of the battery rack and explores its cooling characteristics. Four cases of battery rack configurations are proposed, as demonstrated in Fig. 8. The maximum bulk temperature ($T_{max,bulk}$), and maximum bulk temperature difference $\Delta T = T_{max,bulk} - T_{min,bulk}$, and pressure drop ΔP are used to evaluate the cooling performance of the battery rack. To optimize the structure better, the root-mean-square deviation (*RMSE*) of each duct is used to describe the temperature and mass flow rate distribution uniformity in the structure, where $\dot{V}$ is the flow rate of each layer, $\overline{V}$ is the average flow rate, and n is the layer number.

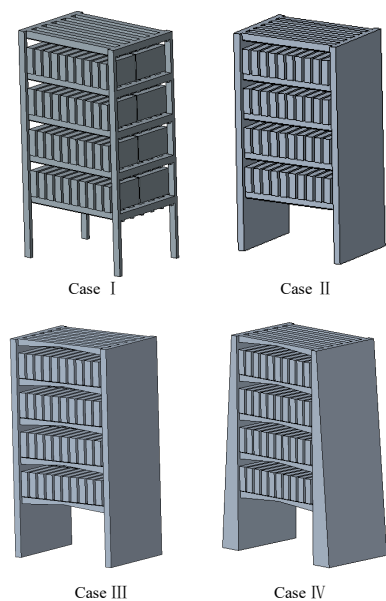$$RMSE = \sqrt{\sum_{1}^{n}(\dot{V} - \overline{V})\frac{1}{N}} \qquad (16)$$

Fig. 8 Schematic diagram of four cases

3.1 First-level flow distribution analysis of four cases

The self-forming battery rack has two levels of flow distribution structure, the first-level flow distribution allocates flow rate between layers, the second-level allocates flow rate between X ducts at each layer. For Case I, there is an extra step of distributing the flow rate from Z-duct to Y-duct, which is also an interlayer flow distribution. The characteristics of the first-level flow distribution can be analyzed from the velocity contour in Fig. 9. It can be seen that the airflow first flows upward along with the Z-direction duct, while Fig. 9a shows that Case I

does not evenly flow into each layer of the X and Y direction duct as expected. Most air flows into the upper layer and then flows out through the nozzles. As can be seen from the histogram in Fig. 10, the upper layer 5 of Case I has the maximum flow rate and layer 2 has the minimum flow rate, and there is a 24.3 g/s difference between layer 2 and layer 5. While Case II shows increasing flow rate trend from the bottom to the upper layer. The flow rate in the upper layer is significantly reduced compared with that in Case I. The distribution between layers is improved but still has poor uniformity. For the first level flow distribution, *RMSEz* was used for evaluation in this paper as shown in Fig. 10. It can be seen that the *RMSEz* of Case II is improved by 6.13 g/s compared to that of Case I. Case III and Case IV show the phenomenon that the flow rate of the first layer is higher and other layers is uniform. The flow distribution of Case IV is more uniform than Case III. This is because the Z-direction duct area of Case III and Case IV reduced proportionally along Z-direction. The shrinking-area Z-direction duct creates high flow resistance near the upper layer and the velocity is low so that the flow between layers is more uniform. The high flowrate in the first layer may also be related to the tilt angle, and reducing the tilt angle may enhance this problem. As shown in Fig. 10, the *RMSEz* ranks as: Case I=9.36 g/s > Case II=3.23 g/s > Case III=1.18 g/s > Case IV=0.19 g/s. Case II changes four Z-direction ducts into two, which greatly improve the uniformity of flow distribution between layers. Changing the duct to the shape of area-shrinking makes the flow distributed uniformly.
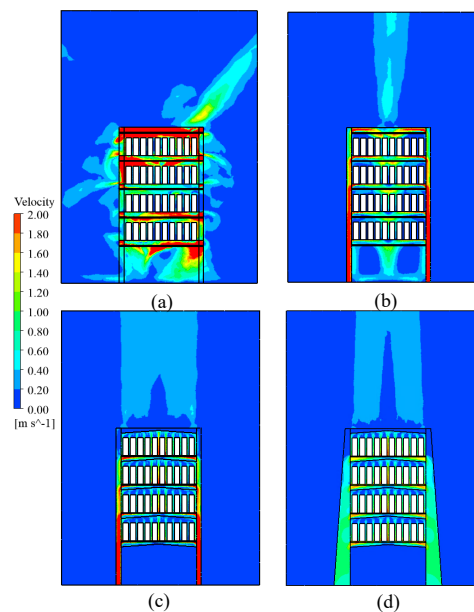

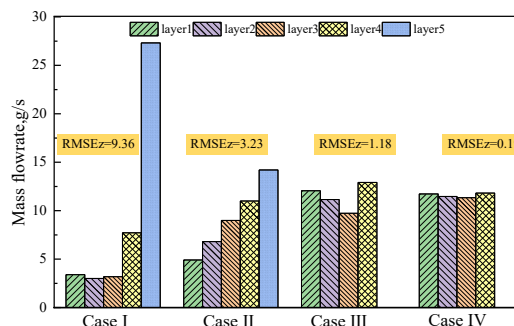**Fig. 9** Velocity contour of four cases in X-Z plane

Fig. 10 Mass flow rate distribution of four cases between layers

It also can be seen from the velocity contour in Fig. 9a and Fig. 9b that most of the air in Case I and Case II flows out of the nozzle from the middle part of the X-direction duct. The flow rate in the central segment is about 10 times that in other areas of the same X-direction duct. This is because the air of the X-direction duct on both sides collides in the middle, and then it diverts the direction flowing out of the nozzle. From Fig. 8c and 8d, the X-direction ducts of Case III and Case IV are mapped as the form of a shrinking-area, and the tilt angle is defined as 4.17°, as noted (Tang *et al*. 2017). To avoid the manufacturing difficulties and uneven jetting caused by changing the nozzle angle, the nozzle is set to spray upward. It also observed from Fig. 9c and 9d velocity contour that the flow distribution of the nozzles in Case III and Case IV is greatly improved compared to Case I and Case II, and that the flow under the same nozzle evenly flushes the spacing of the battery array evenly. Whereas the flow rate in the central segment is about 0.7 times that of the other positions. This is also due to the too large tilt angle. This structure has a plenty of space for improvement.

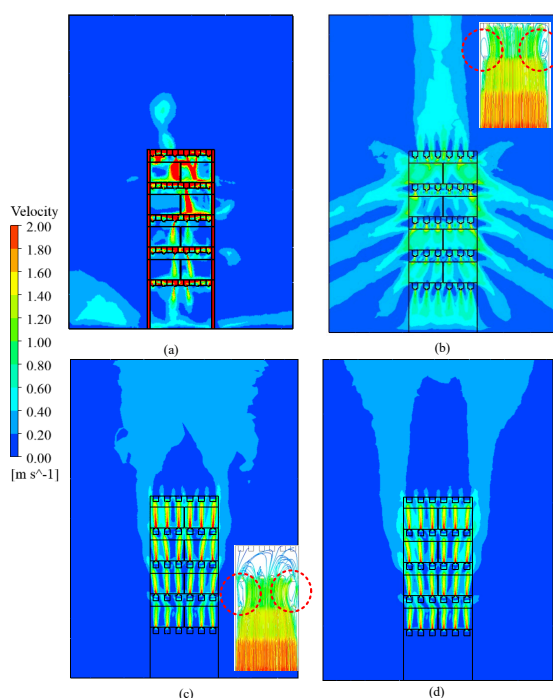### 3.2 Second-level flow distribution analysis of four cases

Fig. 11 Velocity contour of four cases in Y-Z plane. a) Case I; b) Case II; c) Case III; d) Case IV

Figure. 11 shows the uniformity of the secondary flow distribution. As shown in Fig. 11a, Case I is not evenly distributed among X-direction ducts. Air mostly flows out of the X-direction ducts in the central segment of the Y-direction duct. From Fig 12a, it can see that the flow rates of No. 3 and No. 4 ducts are much larger than the other X ducts, especially with the biggest difference in upper layer, where No. 3 occupies 49% of the flow rate of this layer. This is because there are two directions of airflow that affect at the central segment of the Y-direction duct. It is worth noting that the first four layers all have negative flow rate appearing in the sides' X-direction air ducts. This also means that the nozzles not only have no air ejected, but also need to suck air from the opening space. It shows a great non-uniformity of case I. The root mean square error *RMSEx* is adopted to evaluate the flow uniformity between X ducts. The upper layer of Case I with *RMSEx* of 9.36 g/s has the largest dispersion. And the smallest *RMSEx* is 2.24 g/s in the second layer, which also has a high flow dispersion.
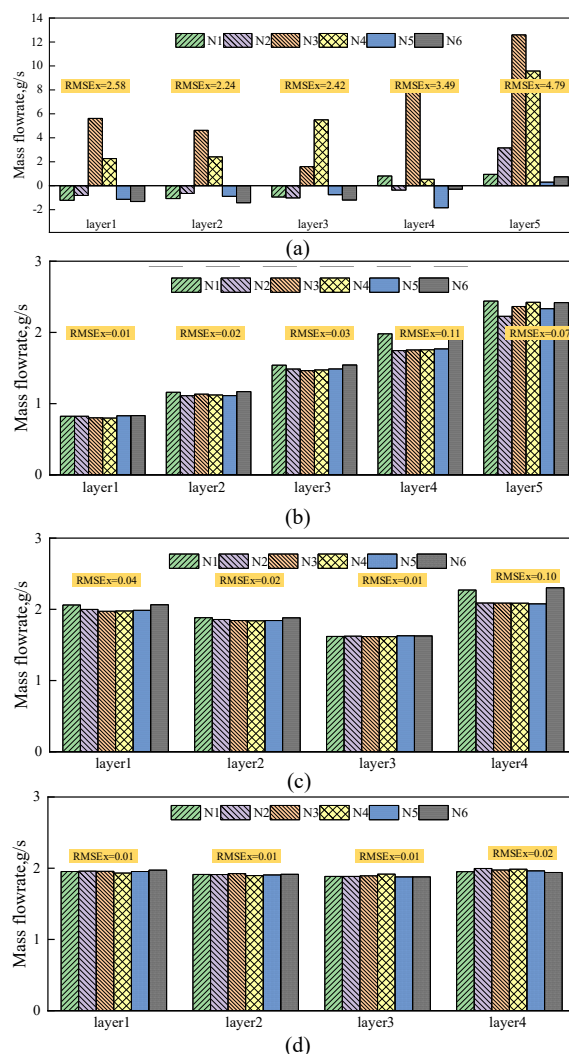

Fig. 12 Mass flow rate distribution histogram of a) Case I; b) Case II; c) Case III; d) Case IV

For Case II, as shown in Fig.11b and 12b, the flow distribution between the X ducts becomes more uneven from the bottom to the upper layer. The uniformity of the X ducts flow in Case II is much improved. The average *RMSEx* for each layer is only 0.048 g/s, and the largest is 0.11 g/s in layer 4. However, each layer has a high flow rate of X ducts on the sides, shown in Fig. 12b. This is because the air was blocked at the upper of the Z duct to create a vortex as shown in Fig. 11b, and the vortex mainly exists near the upper layer and is rotating to the sides' X-ducts. Because the fastest vortex velocities are located in No. 1 and No. 6 of X ducts in layer 4, the X duct on both sides share more air flow. The lower layer has the less influence of vortex. As shown in Fig. 12c, the same situation occurs in Case III, where the fluid is less diverted in the first few layers. Case III has one layer less compared to Case I and Case II, resulting in the air flowing to the upper layer with still high velocity. The fastest velocity of vortex is also located in the fourth layer as shown in Fig. 11c, so the flow rate on both sides of the fourth layer is significantly higher than the others. Thus the largest *RMSEx* was in the upper layer, which is 0.1 g/s. While the average *RMSEx* was 0.043 g/s, which was not significantly different compared to Case II. Case IV has the highest uniformity of flow distribution due to the tapering shape of both Z and X ducts. The average *RMSEx* is 0.013 g/s. The *RMSEx* of four cases ranks as: Case I > Case II> Case III> Case IV.

3.3 Temperature performance of four structures

First of all, from Fig. 13 temperature contour, it can be seen that there is a large temperature deviation in Case I and Case II, and the cell temperature is not only uneven between the layers, but also varies a lot between the cells of each layer. The temperature distribution of Case III and Case IV are more uniform. Fig. 14 shows the average temperature distribution and temperature dispersion $RMSE_T$. As shown in Fig. 13a, the uneven flow distribution of Case I results in non-uniform temperature between batteries. The temperature of each layer decreases from the bottom to the upper layer in the Z direction. From Fig. 14, the $RMSE_T$ reached 4.2 ºC. The battery's lowest bulk temperature $T_{min,bulk}$ is at the upper layer, which is 28.2 ºC. While the bottom layer of the battery has the maximum bulk temperature $T_{max,bulk}$, which is 53.2 ºC. The maximum bulk temperature difference ΔT between batteries is 25 ºC. The pressure drop reaches 136 Pa. The uneven flow distribution between the X-direction ducts results in ΔT of 6.9 ºC within a single battery. During the operation process, the battery temperature should be above 20 °C and below 40 °C, the ΔT between batteries ought to be within 5 °C, and the ΔT within single cells have to be less than 3 °C. It is clear that the Case I battery rack does not meet the requirements for battery safty operation, and there is a risk of thermal runaway during long-term operation.
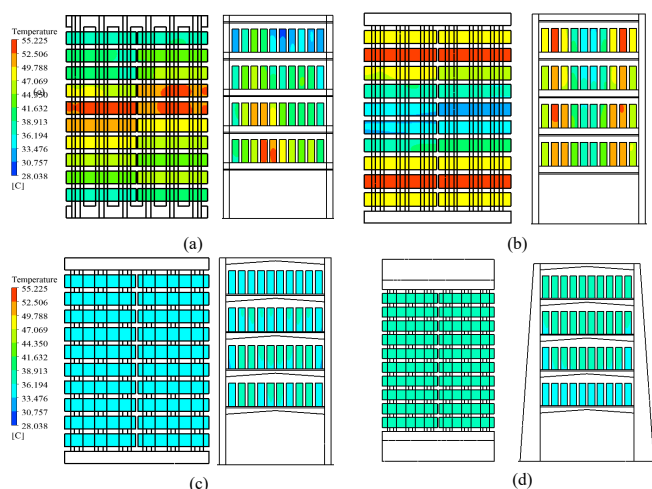

Fig. 13 Battery surface temperature contour of a) Case I; b) Case II; c) Case III; d) Case IV
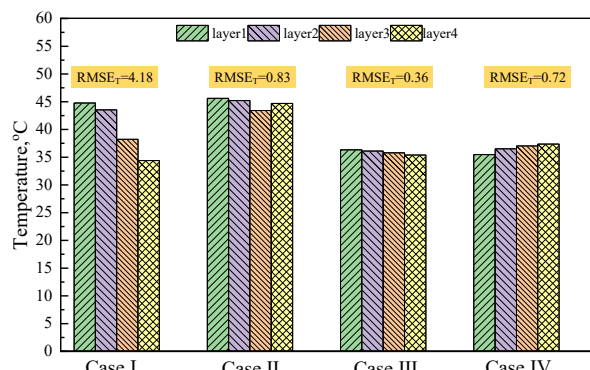

Fig. 14 Layer average temperature distribution histogram of a) Case I; b) Case II; c) Case III; d) Case IV

As shown in Fig. 13b, for Case II, the battery temperature in the middle part of each layer is lower, and the temperature on both sides of the X-direction ducts is higher. The $T_{max,bulk}$ occurs on the upper layer, which is 55.2 ºC. Whilst $T_{min,bulk}$ appears in the central part battery of the first layer, which is 32.6 ºC. The maximum ΔT between batteries and ΔT within single-cell are 22.6 ºC and 13 ºC, respectively. While the third

layer had the lowest average temperature, the first layer had the highest. This is also related to the vortex in the Z duct, and the $RMSE_T$ is 0.8 ºC. Though the temperature distribution is more uniform than Case I, all layers in Case II had an average temperature above 40 ºC. Case II also can't reach the safety standards.

From Fig. 13c, compared with Case I and Case II, Case III's temperature uniformity is greatly improved and the average temperature is under 40 ºC in all layers. The temperature distribution between layers still shows a decreasing trend from bottom to upper and has a more average $RMSE_T$ of 0.36 ºC. The ΔT between the cells is reduced to 2.5 ºC. However, since the flow rate of the first layer is still 1.5 g/s less than the upper layer, the $T_{max,bulk}$ is 39 ºC and appears in the first layer. It is also 16 ºC lower than Case II and within the optimal working temperature range. Further, the $T_{min,bulk}$ is 32.8 ºC, but the ΔT between batteries is 6.2 ºC, which is out of the operational safety requirements. Case IV is shown in Fig. 13d, the temperature of the first layer is lower than that of the upper layer, which also corresponds to the slightly larger flow rate of the first layer. The temperature uniformity of the layers is slightly reduced compared to Case III, but the temperature per layer is still below 40 ºC. The $T_{min,bulk}$ is 34.1 ºC, the $T_{max,bulk}$ is 37.9 ºC, and the ΔT between batteries is 3.8 ºC, while the ΔT within a single battery is 1 ºC. Therefore, Case IV can meet the battery safe operation requirements under low pump power and improve battery safety.
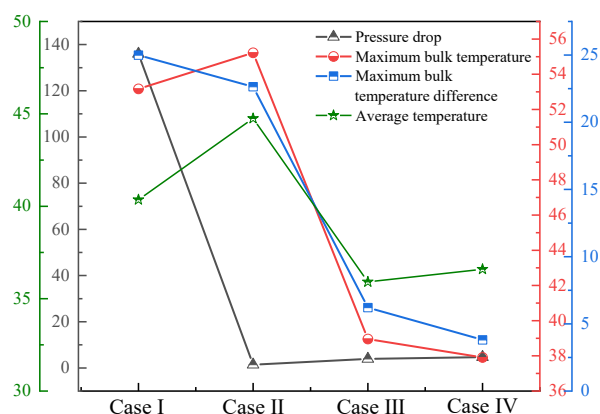
3.4 Temperature performance of four structures

Fig. 15. Comparison of pressure drop ΔP, maximum temperature $T_{max,bulk}$ and temperature difference ΔT for all cases.

According to the previous description, Case IV has the most uniform flow distribution, while the pressure drop is low. It can also be noted from Fig. 15, Case IV likewise has best T_{max} and temperature uniformity among all cases. And only Case IV meets the safe standards of the energy storage battery. Therefore, to obtain detailed cooling performance, the Case IV scheme is used to discharge 80 batteries at 0.5 C and monitor the $T_{max,bulk}$, as illustrated in Fig. 16. Additionally, temperature at the end of discharge is 33.8 ºC, which is within the safe range. The $T_{min,bulk}$ is recorded at about 31.5 ºC, and the maximum bulk temperature difference ΔT between batteries is up to 2.3 ºC, which is lower than the standard. The pressure drop is also up to 4.8 Pa.

A large total mass flow rate V may cause a large flow non-uniformity of Case IV. Therefore, the influence of the total mass flow rate on the maximum volume temperature $T_{max,bulk}$ and pressure drop ΔP is calculated. As presented in Fig. 17a, the $T_{max,bulk}$ decreases logarithmically with the increase of total mass flowrate, and ΔP increases exponentially. When V increases from 46 g/s to 184 g/s, $T_{max,bulk}$ decreases by 7.1 ºC and ΔP increases by 74.3 Pa. However, when V is raised from 184 g/s to 368 g/s, $T_{max,bulk}$ only decreases by 1.2 ºC, and ΔP increases by 237.7 Pa. As a result, an excessively high mass flow rate will result in less temperature reduction while also consuming more pump power.
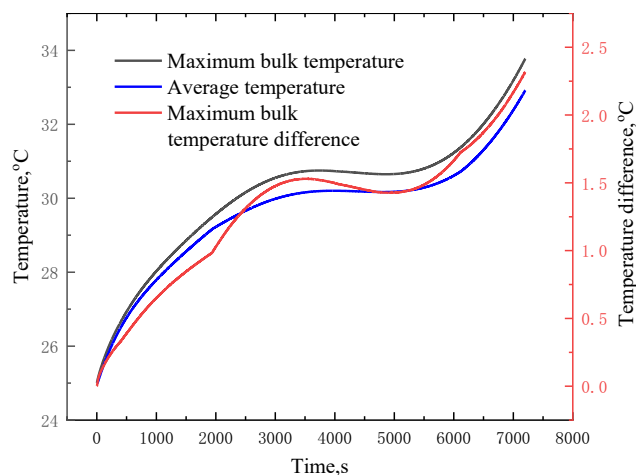
Fig. 16. Temperature variation curve at 0.5C discharge.

As shown in Fig. 17b, maximum bulk temperature difference ΔT and *RMSE* change are similar to T_{max} and pressure drop change. When the total mass flowrate V is lessened, the increase in flow rate has a significant influence on ΔT improvement. For instance, when the flow rate is 92 g/s, the ΔT of the battery pack is only 2 °C, and is 1.8 °C lower than that of 46 g/s. However, the ΔT decreases by less than 12% when V continues to increase. Therefore, operating at a 92 g/s flowrate will achieves a better cooling performance. It is also observed from Fig. 17b that *RMSE* also increases exponentially with the increase of V, which means that as the total mass flow rate increases, the flow deviation of each layer becomes larger, but this rise is acceptable. Where the flow deviation is on the order of 2 g/s, which is sufficient to demonstrate the superiority of the Case IV structure.
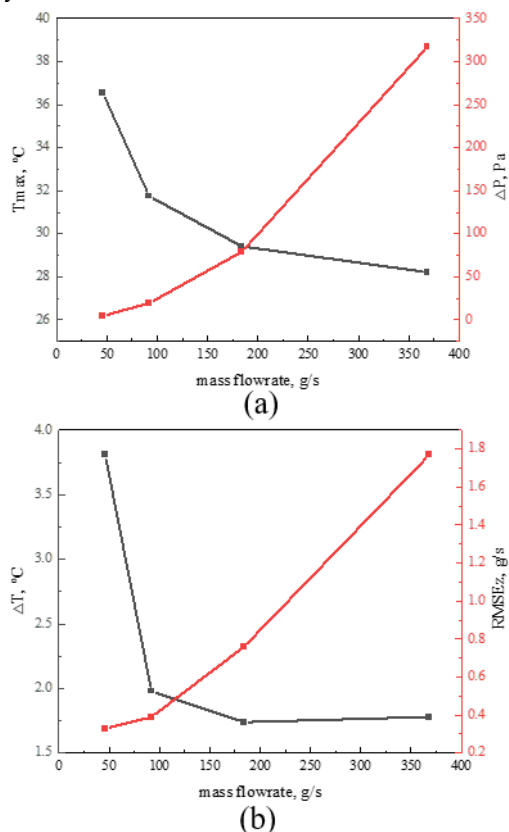

Fig. 17. a) maximum bulk temperature $T_{max,bulk}$, pressure drop ΔP; b) temperature difference ΔT, $RMSEz$ curve with the flow rate.

4. CONCLUSIONS

In this study, a novel self-forming air-cooling rack is proposed, which uses the same battery rack structure of the battery rack itself as an airflow channel to improve the integrity of the storage battery rack integration and the battery temperature uniformity. It provides an effective and potential thermal management method for the large LIB energy storage system. The conclusions are as follows:

1. The shrinking-area of the Z-direction duct and X-direction duct of the Case IV can evenly distribute the air in all branch ducts. Thus, the battery can be evenly cooled. The battery array is placed on X-direction ducts, and the nozzles can evenly supply cooling air equally through battery spacing.
2. The maximum temperature can be maintained at 33.8 °C at 0.5 C under the 46 g/s flowrate. Where the maximum bulk temperature difference between batteries and inside a single battery is less than 3.8 °C and 1 °C, respectively. The pressure drop is only 4.8 Pa.
3. With the increase of total mass flowrate, the non-uniformity of flow rate in the battery rack branch ducts gradually increases. The larger the total mass flowrate is the more uniform the flow rate distribution is. What's more, Case IV achieves optimal cooling performance at a 92 g/s flowrate, under which the maximum bulk temperature is 31.8 °C with the pressure drop of 19.5 Pa.

NOMENCLATURE

c_p	specific heat (J/kg·K)
V	total mass flowrate (g/s)
R	resistance (Ω)
t	time (s)
T	temperature (°C)
v	velocity (m/s)
x, y, z	coordinate
SOC	state of charge
OCV	open circuit voltage(V)
P	pressure(Pa)
q	heat flux (W/m2)
Greek Symbols	
λ	thermal conductivity (W/m·K)
ρ	density (kg/m³)
Subscripts	
max	maximum
min	minimum
bulk	battery bulk
a	air
e	electricity
bat	battery
irr	irreversible
rev	reversible

REFERENCES

Ashkboos, P., A. Yousefi, and E. Houshfar. 2021. "Design improvement of thermal management for Li-ion battery energy storage systems." *Sustainable Energy Technologies and Assessments*, 44: 101094. https://doi.org/10.1016/j.seta.2021.101094.

Bandhauer, T. M., S. Garimella, and T. F. Fuller. 2011. "A Critical Review of Thermal Issues in Lithium-Ion Batteries." *J. Electrochem. Soc.*, 158 (3): R1.

https://doi.org/10.1149/1.3515880.

Basu, S., K. S. Hariharan, S. M. Kolake, T. Song, D. K. Sohn, and T. Yeo. 2016. "Coupled electrochemical thermal modelling of a novel Li-ion battery pack thermal management system." *Applied Energy*, 181: 1–13. https://doi.org/10.1016/j.apenergy.2016.08.049.

Fan, L., J. M. Khodadadi, and A. A. Pesaran. 2013. "A parametric study on thermal management of an air-cooled lithium-ion battery module for plug-in hybrid electric vehicles." *Journal of Power Sources*, 238: 301–312.
https://doi.org/10.1016/j.jpowsour.2013.03.050.

Fathabadi, H. 2014. "A novel design including cooling media for Lithium-ion batteries pack used in hybrid and electric vehicles." *Journal of Power Sources*, 245: 495–500.
https://doi.org/10.1016/j.jpowsour.2013.06.160.

Fathima, A. H., and K. Palanismay. 2017. "Modeling and Operation of a Vanadium Redox Flow Battery for PV Applications." *Energy Procedia*, 117: 607–614.
https://doi.org/10.1016/j.egypro.2017.05.157.

Gümüşsu, E., Ö. Ekici, and M. Köksal. 2017. "3-D CFD modeling and experimental testing of thermal behavior of a Li-Ion battery." *Applied Thermal Engineering*, 120: 484–495.
https://doi.org/10.1016/j.applthermaleng.2017.04.017.

Hémery, C.-V., F. Pra, J.-F. Robin, and P. Marty. 2014. "Experimental performances of a battery thermal management system using a phase change material." *Journal of Power Sources*, 270: 349–358.
https://doi.org/10.1016/j.jpowsour.2014.07.147.

Hong, S., X. Zhang, K. Chen, and S. Wang. 2018. "Design of flow configuration for parallel air-cooled battery thermal management system with secondary vent." *International Journal of Heat and Mass Transfer*, 116: 1204–1212.
https://doi.org/10.1016/j.ijheatmasstransfer.2017.09.092.

Hussain, A., C. Y. Tso, and C. Y. H. Chao. 2016. "Experimental investigation of a passive thermal management system for high-powered lithium ion batteries using nickel foam-paraffin composite." *Energy*, 115: 209–218.
https://doi.org/10.1016/j.energy.2016.09.008.

Kalogiannis, T., M. Akbarzadeh, M. S. Hosen, H. Behi, L. De Sutter, L. Jin, J. Jaguemont, J. Van Mierlo, and M. Berecibar. 2022. "Effects analysis on energy density optimization and thermal efficiency enhancement of the air-cooled Li-ion battery modules." *Journal of Energy Storage*, 48: 103847.
https://doi.org/10.1016/j.est.2021.103847.

Killer, M., M. Farrokhseresht, and N. G. Paterakis. 2020. "Implementation of large-scale Li-ion battery energy storage systems within the EMEA region." *Applied Energy*, 260: 114166.
https://doi.org/10.1016/j.apenergy.2019.114166.

Kim, J., J. Oh, and H. Lee. 2019. "Review on battery thermal management system for electric vehicles." *Applied Thermal Engineering*, 149: 192–212. https://doi.org/10.1016/j.applthermaleng.2018.12.020.

Lan, C., J. Xu, Y. Qiao, and Y. Ma. 2016. "Thermal management for high power lithium-ion battery by minichannel aluminum tubes." *Applied Thermal Engineering*, 101: 284–292.
https://doi.org/10.1016/j.applthermaleng.2016.02.070.

Le, Q., Q. Shi, Q. Liu, X. Yao, X. Ju, and C. Xu. 2022. "Numerical investigation on manifold immersion cooling scheme for lithium ion battery thermal management application." *International Journal of Heat and Mass Transfer*, 190: 122750.
https://doi.org/10.1016/j.ijheatmasstransfer.2022.122750.

Lei, S., Y. Shi, and G. Chen. 2020. "A lithium-ion battery-thermal-

management design based on phase-change-material thermal storage and spray cooling." *Applied Thermal Engineering*, 168: 114792.
https://doi.org/10.1016/j.applthermaleng.2019.114792.

Lou, T. T., W. G. Zhang, H. Y. Guo, and J. S. Wang. 2012. "The Internal Resistance Characteristics of Lithium-Ion Battery Based on HPPC Method." *AMR*, 455–456: 246–251.
https://doi.org/10.4028/www.scientific.net/AMR.455-456.246.

Mahamud, R., and C. Park. 2011. "Reciprocating air flow for Li-ion battery thermal management to improve temperature uniformity." *Journal of Power Sources*, 196 (13): 5685–5696.
https://doi.org/10.1016/j.jpowsour.2011.02.076.

Park, H. 2013. "A design of air flow configuration for cooling lithium ion battery in hybrid electric vehicles." *Journal of Power Sources*, 239: 30–36.
https://doi.org/10.1016/j.jpowsour.2013.03.102.

Pesaran, A. A. 2002. "Battery thermal models for hybrid vehicle simulations." *Journal of Power Sources*, 110 (2): 377–382.
https://doi.org/10.1016/S0378-7753(02)00200-8.

Piao, N., X. Gao, H. Yang, Z. Guo, G. Hu, H.-M. Cheng, and F. Li. 2022. "Challenges and development of lithium-ion batteries for low temperature environments." *eTransportation*, 11: 100145.
https://doi.org/10.1016/j.etran.2021.100145.

Rao, Z., and S. Wang. 2011. "A review of power battery thermal energy management." *Renewable and Sustainable Energy Reviews*, 15 (9): 4554–4571.
https://doi.org/10.1016/j.rser.2011.07.096.

Saw, L. H., Y. Ye, A. A. O. Tay, W. T. Chong, S. H. Kuan, and M. C. Yew. 2016. "Computational fluid dynamic and thermal analysis of Lithium-ion battery pack with air cooling." *Applied Energy*, 177: 783–792.
https://doi.org/10.1016/j.apenergy.2016.05.122.

Schimpe, M., M. Naumann, N. Truong, H. C. Hesse, S. Santhanagopalan, A. Saxon, and A. Jossen. 2018. "Energy efficiency evaluation of a stationary lithium-ion battery container storage system via electro-thermal modeling and detailed component analysis." *Applied Energy*, 210: 211–229.
https://doi.org/10.1016/j.apenergy.2017.10.129.

Sun, H., and R. Dixon. 2014. "Development of cooling strategy for an air cooled lithium-ion battery pack." *Journal of Power Sources*, 272: 404–414.
https://doi.org/10.1016/j.jpowsour.2014.08.107.

Tang, W., L. Sun, H. Liu, G. Xie, Z. Mo, and J. Tang. 2017. "Improvement of flow distribution and heat transfer performance of a self-similarity heat sink with a modification to its structure." *Applied Thermal Engineering*, 121: 163–171.
https://doi.org/10.1016/j.applthermaleng.2017.04.051.

Tao, F., W. Zhang, D. Guo, W. Cao, L. Sun, and F. Jiang. 2020. "Thermofluidic modeling and temperature monitoring of Li-ion battery energy storage system." *Applied Thermal Engineering*, 181: 116026.
https://doi.org/10.1016/j.applthermaleng.2020.116026.

Tong, W., K. Somasundaram, E. Birgersson, A. S. Mujumdar, and C. Yap. 2015. "Numerical investigation of water cooling for a lithium-ion bipolar battery pack." *International Journal of Thermal Sciences*, 94: 259–269.
https://doi.org/10.1016/j.ijthermalsci.2015.03.005.

Tong, W., K. Somasundaram, E. Birgersson, A. S. Mujumdar, and C. Yap. 2016. "Thermo-electrochemical model for forced convection air cooling of a lithium-ion battery module." *Applied Thermal Engineering*, 99: 672–682.
https://doi.org/10.1016/j.applthermaleng.2016.01.050.

Tran, T.-H., S. Harmand, and B. Sahut. 2014. "Experimental investigation on heat pipe cooling for Hybrid Electric Vehicle and Electric Vehicle lithium-ion battery." *Journal of Power Sources*, 265: 262–272. https://doi.org/10.1016/j.jpowsour.2014.04.130.

Väyrynen, A., and J. Salminen. 2012. "Lithium ion battery production." *The Journal of Chemical Thermodynamics*, 46: 80–85. https://doi.org/10.1016/j.jct.2011.09.005.

Wang, T., K. J. Tseng, and J. Zhao. 2015a. "Development of efficient air-cooling strategies for lithium-ion battery module based on empirical heat source model." *Applied Thermal Engineering*, 90: 521–529. https://doi.org/10.1016/j.applthermaleng.2015.07.033.

Wang, Z., Z. Zhang, L. Jia, and L. Yang. 2015b. "Paraffin and paraffin/aluminum foam composite phase change material heat storage experimental study based on thermal management of Li-ion battery." *Applied Thermal Engineering*, 78: 428–436. https://doi.org/10.1016/j.applthermaleng.2015.01.009.

Xie, J., Z. Ge, M. Zang, and S. Wang. 2017. "Structural optimization of lithium-ion battery pack with forced air cooling system." *Applied Thermal Engineering*, 126: 583–593. https://doi.org/10.1016/j.applthermaleng.2017.07.143.

Yang, N., X. Zhang, G. Li, and D. Hua. 2015. "Assessment of the forced air-cooling performance for cylindrical lithium-ion battery packs: A comparative analysis between aligned and staggered cell arrangements." *Applied Thermal Engineering*, 80: 55–65. https://doi.org/10.1016/j.applthermaleng.2015.01.049.

Zhang, J., J. Huang, Z. Li, B. Wu, Z. Nie, Y. Sun, F. An, and N. Wu. 2014. "Comparison and validation of methods for estimating heat generation rate of large-format lithium-ion batteries." *J Therm Anal Calorim*, 117 (1): 447–461. https://doi.org/10.1007/s10973-014-3672-z.

Zhang, T., Q. Gao, G. Wang, Y. Gu, Y. Wang, W. Bao, and D. Zhang. 2017. "Investigation on the promotion of temperature uniformity for the designed battery pack with liquid flow in cooling process." *Applied Thermal Engineering*, 116: 655–662. https://doi.org/10.1016/j.applthermaleng.2017.01.069.

Zhao, R., J. Gu, and J. Liu. 2015. "An experimental study of heat pipe thermal management system with wet cooling method for lithium ion batteries." *Journal of Power Sources*, 273: 1089–1097. https://doi.org/10.1016/j.jpowsour.2014.10.007.

Zhou, H., F. Zhou, L. Xu, J. Kong, and QingxinYang. 2019. "Thermal performance of cylindrical Lithium-ion battery thermal management system based on air distribution pipe." *International Journal of Heat and Mass Transfer*, 131: 984–998. https://doi.org/10.1016/j.ijheatmasstransfer.2018.11.116.

Zhu, C., X. Li, L. Song, and L. Xiang. 2013. "Development of a theoretically based thermal model for lithium ion battery pack." *Journal of Power Sources*, 223: 155–164. https://doi.org/10.1016/j.jpowsour.2012.09.035.